PAPER

Check for updates

Selection of a compatible electron transport layer and hole transport layer for the mixed perovskite $FA_{0.85}Cs_{0.15}Pb$ ($I_{0.85}Br_{0.15}$)$_3$, towards achieving novel structure and high-efficiency perovskite solar cells: a detailed numerical study by SCAPS-1D†

Md. Bulu Rahman,[a] Noor-E-Ashrafi,[a] Md. Helal Miah, [iD] *[a] Mayeen Uddin Khandaker[b] and Mohammad Aminul Islam*[c]

The first and foremost intent of our present study is to design a perovskite solar cell favorable for realistic applications with excellent efficiency by utilizing SCAPS-1D. To ensure this motive, the detection of a compatible electron transport layer (ETL) and hole transport layer (HTL) for the suggested mixed perovskite layer entitled $FA_{0.85}Cs_{0.15}Pb$ ($I_{0.85}Br_{0.15}$)$_3$ (MPL) was carried out, employing diver ETLs such as SnO_2, PCBM, TiO_2, ZnO, CdS, WO_3 and WS_2, and HTLs such as Spiro-OMeTAD, P3HT, CuO, Cu_2O, CuI, and MoO_3. The attained simulated results, especially for FTO/SnO_2/$FA_{0.85}Cs_{0.15}Pb$ ($I_{0.85}Br_{0.15}$)$_3$/Spiro-OMeTAD/Au, have been authenticated by the theoretical and experimental data, which endorse our simulation process. From the detailed numerical analysis, WS_2 and MoO_3 were chosen as ETL and HTL, respectively, for designing the proposed novel structure of $FA_{0.85}Cs_{0.15}Pb$ ($I_{0.85}Br_{0.15}$)$_3$-based perovskite solar cells. With the inspection of several parameters such as variation of the thickness of $FA_{0.85}Cs_{0.15}Pb$ ($I_{0.85}Br_{0.15}$)$_3$, WS_2, and MoO_3 including different defect densities, the novel proposed structure has been optimized, and a noteworthy efficiency of 23.39% was achieved with the photovoltaic parameters of V_{OC} = 1.07 V, J_{SC} = 21.83 mA cm^{-2}, and FF = 73.41%. The dark J−V analysis unraveled the reasons for the excellent photovoltaic parameters of our optimized structure. Furthermore, the scrutinizing of QE, C−V, Mott−Schottky plot, and the impact of the hysteresis of the optimized structure was executed for further investigation. Our overall investigation disclosed the fact that the proposed novel structure (FTO/WS_2/$FA_{0.85}Cs_{0.15}Pb$ ($I_{0.85}Br_{0.15}$)$_3$/MoO_3/Au) can be attested as a supreme structure for perovskite solar cells with greater efficiency as well as admissible for practical purposes.

1. Introduction

Perovskites with formula AMX_3 (where A, M, and X are organic/inorganic cations, metal cations, and oxygen/halogen anions, respectively) are extremely lucrative materials in the sector of photovoltaic technology owing to their intriguing optoelectronic properties such as tunable band gap, high absorption coefficients, large charge carrier diffusion lengths and high mobility, and ambipolar charge transportation.[1,2] Kojima et al.[3] first utilized a perovskite material named $CH_3NH_3PbI_3$ for

photovoltaic applications and obtained a power conversion efficiency (PCE) of 3.81%. Perovskite material-based solar cells are gaining substantial attention in terms of efficiency, and throwing challenges to the existing solar cells including silicon-based solar cells. Recently, Min et al.[4] reported 25.8% PCE by employing $FAPbI_3$-based solar cells. However, Si-based solar cells are still overshadowing other PSCs due to their high PCE (26.7%[5]) as well as longevity. In addition to this, a group of scientists from Helmholtz-Zentrum Berlin fabricated tandem solar cells by adopting silicon and perovskite material and attained a world record PCE of 32.5%, which ultimately glorifies the necessity of perovskite material. The composition of the stoichiometric structure of perovskite AMX_3 governs the energy band gap, crystal phase, stability as well as performance in photovoltaic applications. The Goldschmidt geometric tolerance factor, $t = \dfrac{r_A + r_X}{\sqrt{r_M + r_X}}$ where r_A, r_M and r_X are the effective ionic radii for A, M and X, respectively, determines the formability and stability of a perovskite structure.[6] The tolerance

[a]Department of Physics, Bangabandhu Sheikh Mujibur Rahman Science and Technology University, Gopalganj 8100, Bangladesh

[b]Centre for Applied Physics and Radiation Technologies, School of Engineering and Technology, Sunway University, 47500 Bandar Sunway, Selangor, Malaysia

[c]Department of Electrical Engineering, Faculty of Engineering, Universiti Malaya, Jalan Universiti, 50603 Kuala Lumpur, Malaysia

† Electronic supplementary information (ESI) available. See DOI: https://doi.org/10.1039/d3ra02170j

factor can be aligned within 0.8–1.0 for steady and worthy structure in photovoltaic technology by partially or fully supplanting the ions of various sites in the AMX_3 structure. In a recent study, Liu et al.[7] synthesized a perovskite solar cell (PSC) of structure $FTO/NiO_x/CsPbI_3/ZnO/ITO$ in which the MA cation was substituted by Cs in the perovskite material. They reported a PCE of 16.04%, which was capable to retain 90% PCE even after 3000 hours of constant lighting and heating. In another study, Saliba et al.[8] fabricated mixed perovskite structures of $Cs_x(MA_{0.17}FA_{0.83})_{1-x}Pb(I_{0.83}Br_{0.17})_3$ and obtained a PCE of 21.1% by utilizing this structure in a PSC. The reported structure was able to hold nearly 97% of its initial efficiency after 250 hours of light exposure.

In another extensive study carried out by Liu et al.[9] where they developed a PSC by applying $Cs_{0.05}FA_{0.79}MA_{0.16}PbI_{2.49}Br_{0.51}$ perovskite structure and claimed that 93% of the initial PCE (21.1%) was maintained under humidity (30–60%) for 1200 hours.

Besides the perovskite material, an efficient PSC has a dependency on ETL, HTL, and the interfacial ETL/perovskite layer and perovskite layer/HTL layers.[10] Semiconducting materials are reckoned as charge transport materials that render better transparency in the solar spectrum, broad bandgap, high mobility of charge carriers, and greater thermal and chemical stability. ETL, which extract photo-generated electrons from the perovskite layer and precludes the transfer of hole towards the electrode via ETL, and eventually electron–hole recombination at the interfaces of the perovskite layer gets inhibited. One of the crucial features of selecting ETL is that the energy levels of the material should be compatible with perovskite material to extract electrons and preclude holes. Normally, n-type semiconducting materials such as ZnO, SnO_2, CdS, TiO_2, WO_3, WS_2, PCBM, and TMD are broadly esteemed as the ETL. By replacing or modifying the ETL, the overall stability and performance of the PSC can be greatly influenced. Pathak et al.[11] modified the ETL of the device $Spiro-OMeTAD/CH_3NH_3PbI_3/TiO_2$ by doping it with Al (0.3 mol%), and subsequently, PCE was increased by approximately 24%. Another analysis was conducted by Song et al.,[12] in which, TiO_2 was replaced with SnO_2 of the architecture $Spiro-OMeTAD/CH_3NH_3PbI_3/TiO_2$ and substantiated 13% PCE. They also emphasized that PSC with SnO_2-based solar cells are more stable in comparison with TiO_2 based solar cells. In a recent study, Min et al.[4] achieved highest PCE (25.8%) by employing SnO_2 as an ETL.

HTL provides a pivotal role in extracting photo-generated holes from the perovskite layer and acts as a blocking element for electrons toward the metal electrode. One of the important aspects of choosing HTL is that the energy levels of the material should be relevant to perovskite material for the purpose of hole extraction and blocking the electron. Usually, HTL is a p-type semiconducting material including Spiro-OMeTAD, MoO_3, Cu_2O, PEDOT:PSS, CuSCN, CuI, PTAA, CuO, and P3HT.

The first ever solid-state HTL (Spiro-OMeTAD) was utilized by Kim[20] et al. in Kojima's first perovskite, and enhancement of PCE from 3.8% to 9.7% was observed. By substituting or modifying the HTL layer, the overall performance of the PSC can be influenced to some extent. By applying MoO_3 instead of PEDOT:PSS and WO_3 as the HTL, Tseng et al. synthesize PSCs with the active layer of $CH_3NH_3PbI_3$ and obtained 13.1% PCE.[21] Their analysis distinctively disclosed that in terms of overall performance, the devices manufactured with the MoO_3 film are better than the devices employed with WO_3 and PEDOT:PSS as the HTL. Since MoO_3 has high work function (6.9 eV), better conductivity (1.2×10^{-7} sm^{-1}) as well as a larger band-gap (>3 eV, no absorption in the visible-infrared range), it has established itself as a competent HTL.[22] A schematic diagram of the perovskite structure, n–i–p structured PSC, and equivalent circuit of the PSC are portrayed in Fig. 1.

In this theoretical work, we have executed a computational analysis by utilizing a solar cell capacitance simulator (SCAPS 1D-3.3.1.0) for choosing compatible ETL and HTL with $FA_{0.85}Cs_{0.15}Pb(I_{0.85}Br_{0.15})_3$ (MPL) as the mixed perovskite layer. For this motive, primarily, we selected SnO_2, PCBM, TiO_2, ZnO, CdS, WO_3, and WS_2 as ETLs. Likewise, Spiro-OMeTAD, P3HT, CuO, Cu_2O, CuI, and MoO_3 were chosen as HTLs in our proposed n–i–p structure. All initial input physical parameters (IIPPs) of ETL, HTL, and MPL utilized in this simulated study were collected from the previously reported experimental and simulated data. Our prime focus for this research was to identify the structure that serves the best performance. Herein, 42 structures have been formulated by using the aforementioned ETLs and HTLs with MPL, and eventually, the preferred one was found as well. Finally, we have probed the effect of changing thickness, the defect density of MPL, and interfacial defects on our best structure ($FTO/WS_2/MPL/MoO_3/Au$). In addition, the impact of ETL's shallow uniform donor density on the C–V and M–S plots of the optimized structure was scrutinized. Moreover, QE analysis and the hysteresis effect of the optimized structure were
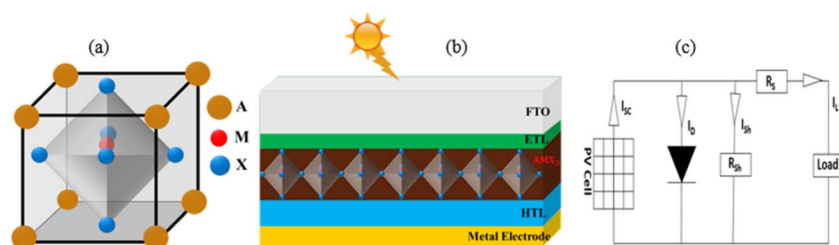

Fig. 1 A schematic diagram of (a) perovskite structure, (b) n–i–p structure of PSC, and (c) equivalent circuit of the PSC.

dissected. Finally, the dark *J–V* analysis was executed to unravel the reasons behind the tremendous photovoltaic parameters of our optimized structure. To the best of our knowledge, this is the first-ever comprehensive study on this unique structure.

2. Computational details

SCAPS, developed by the University of Gent, is a one-dimensional and proficient solar cell simulator among other simulators (SILVACO, ATLAS, AMPS, COMSOL, *etc*)[23–25] and it is widely used to realize the essence of energy band structure, *I–V* characteristics, *C–V* analysis, M–S analysis, doping profile, C-f study, spectral response, *etc.*, of a solar cell. SCAPS-1D is governed by three fundamental eqn (i)–(iii) named continuity equations for holes and electrons, and Poisson's equations to fortuitously complete its task under equilibrium conditions.

$$\frac{dn_p}{dt} = G_n - \frac{n_p - n_{p0}}{\tau_n} + n_p \; \mu_n \; \frac{d\xi}{dx} + \mu_n \xi \frac{dn_p}{dx} + D_n \frac{d^2 n_p}{dx^2} \quad (i)$$

$$\frac{dp_n}{dt} = G_p - \frac{p_n - p_{n0}}{\tau_p} + p_n \mu_p \; \frac{d\xi}{dx} + \mu_p \xi \frac{dp_n}{dx} + D_p \frac{d^2 p_n}{dx^2} \quad (ii)$$

$$\frac{d}{dx}\left(-\varepsilon(x)\frac{d\psi}{dx}\right) = q[p(x) - n(x) + N_D^+(x) - N_A^-(x) + P_t(x) - n_t(x)]$$

$$(iii)$$

where ξ represents the electric field, ε represents permittivity, q is the electronic charge, τ is the carrier lifetime, charge mobilities are indicated by μ, shallow acceptor and shallow donor concentrations are represented N_A and N_D, respectively, D represents the diffusion coefficient of the charge carrier, the charge carrier generation rate is indicated by G, and defect densities of electrons and holes are mentioned by $n_t(x)$ and $p_t(x)$.

3. Results and discussions

In a previous study, Karthick *et al.*[13] synthesized FTO/SnO$_2$/ FA$_{0.85}$Cs$_{0.15}$Pb(I$_{0.85}$Br$_{0.15}$)$_3$/Spiro-OMeTAD/Au-based PSC structure and obtained V_{OC} = 1 V, J_{sc} = 22.6 mA cm^{-2}, FF = 64.4% and PCE = 15.1%. We simulated this structure by using SCAPS to corroborate and compare it with the experimental results. In this simulation, we considered the realistic facts by inserting bulk defects, amphoteric defects, interfacial defects, resistance, *etc.*, and the rest of the IIPPs of the different layers were rendered from different published studies, as shown in Table 1. We maintained the following data in all defect layers for all simulations: the defect type was neutral, energetic distribution was Gaussian, characteristic energy was 0.1 eV, and energy level with respect to reference 0.6 eV and electron/hole capture cross-section 10^{-15} cm^2. We also added interfacial defects at the MPL/ETL and MPL/HTL layers with 2 × 10^{11} cm^{-3} and 2 × 10^{10} cm^{-3}, respectively, in which the electron/hole capture cross section was 10^{-19} cm^2. In addition to that, amphoteric defect of 2 × 10^{15} cm^{-3} was included in the proposed MPL. Furthermore, we performed the simulation by considering constant light illumination of 1000 Watt per m^2 at 1.5 AM ranging from 300–1000 at a temperature of 300 K, series resistance of 3 Ω cm^2, and shunt resistance of 5000 Ω cm^2.

The obtained photovoltaic parameters (PPs) of the structured PSC (S1) were as follows V_{OC} = 0.96 V, J_{SC} = 20.03 mA cm^{-2}, FF = 53.84% and PCE = 14.12%. This simulated result is consistent with the aforementioned experimental results, which vindicated the validity of our simulation.

To observe the finest structures with performance, 42 structures were constructed and simulated by varying different ETLs and HTLs with the aforementioned proposed MPL. The IIPPs of ETLs and HTLs are tabulated in Tables 1 and 2. The simulated results of the 42 structures are displayed in Tables 3 and TSI 01.† Different values of PPs were demonstrated by dissimilar structures depending on the band alignment (as

Table 1 IIPPs for each layer of the PSC collected from ref. 13

Parameters	FTO	SnO$_2$	FA$_{0.85}$Cs$_{0.15}$Pb (I$_{0.85}$Br$_{0.15}$)$_3$	Spiro-OMeTAD	Au
Thickness (t) in nm	500	70	350	165	—
Band gap (E_g) in eV	3.5	3.5	1.59	2.9	—
Electron affinity (χ) in eV	4	4	4.09	2.2	—
Dielectric permittivity (ε_r)	9	9	6.6	3	—
CB effective density of states (N_c) in cm^{-3}	2.2 × 10^{18}	2.2 × 10^{17}	2 × 10^{19}	2.2 × 10^{18}	—
VB effective density of states (N_v) in cm^{-3}	2.2 × 10^{18}	2.2 × 10^{17}	2 × 10^{18}	2.2 × 10^{18}	—
Electron thermal velocity (V_e) in cm s^{-1}	1 × 10^7	1 × 10^7	1 × 10^7	1 × 10^7	—
Hole thermal velocity (V_h) in cm s^{-1}	1 × 10^7	1 × 10^7	1 × 10^7	1 × 10^7	—
Electron mobility (μ_e) in cm^2 V^{-1} s^{-1}	20	20	8.16	0.0001	—
Hole mobility (μ_h) in cm^2 V^{-1} s^{-1}	10	10	2	0.0001	—
Shallow uniform acceptor density (N_A) in cm^{-3}	0	0	1.3 × 10^{16}	1.3 × 10^{18}	—
Shallow uniform donor density (N_D) in cm^{-3}	1 × 10^{15}	1 × 10^{15}	1.3 × 10^{16}	0	—
Defect density (N_t) in cm^{-3}	1 × 10^{18}	1 × 10^{18}	4 × 10^{13}	1 × 10^{15}	—
Amphoteric defect density (ADD) in cm^{-3}	—	—	2 × 10^{15}	—	—
Work function (φ) in (eV)	—	—	—	—	5.3

© 2023 The Author(s). Published by the Royal Society of Chemistry

Paper

Table 2 IIPPs of ETLs and HTLs

	ETLs						HTLS				
Parameters	PCBM	TiO$_2$	ZnO	CdS	WO$_3$	WS$_2$	P3HT	CuO	Cu$_2$O	CuI	MoO$_3$
t (nm)	70	70	70	70	70	70	165	165	165	165	165
E_g (eV)	2	3.2	3.3	2.4	2.6	1.8	2	1.48	2.17	3.1	3
χ (eV)	4.2	4.1	4.1	4.18	3.8	3.95	3.2	4.07	3.2	2.1	2.5
ε_r	3.9	9	9	10	4.8	13.6	3	18.1	7.11	6.5	12.5
N_c (cm^{-3})	2.5×10^{21}	2.2×10^{18}	2.2×10^{18}	2.2×10^{18}	2.2×10^{21}	2.2×10^{17}	1×10^{20}	2.1×10^{19}	2×10^{17}	2.8×10^{19}	2.2×10^{18}
N_v (cm^{-3})	2.5×10^{21}	1×10^{19}	1.9×10^{19}	1.9×10^{19}	2.2×10^{21}	2.2×10^{16}	1×10^{20}	5.5×10^{19}	1.1×10^{19}	1×10^{19}	1.8×10^{19}
V_e (cm s^{-1})	1×10^7	1×10^7	1×10^7	1×10^7	1×10^7	1×10^7	1×10^7	1×10^7	1×10^7	1×10^7	1×10^7
V_h (cm s^{-1})	1×10^7	1×10^7	1×10^7	1×10^7	1×10^7	1×10^7	1×10^7	1×10^7	1×10^7	1×10^7	1×10^7
μ_e (cm^2 V^{-1} s^{-1})	0.2	20	100	100	30	100	1×10^{-4}	100	200	100	25
μ_h (cm^2 V^{-1} s^{-1})	0.2	10	25	25	30	100	1×10^{-4}	0.1	80	43.9	100
N_A (cm^{-3})	0	0	0	0	0	0	1×10^{16}	1×10^{16}	1×10^{18}	1×10^{18}	1×10^{18}
N_D (cm^{-3})	2.93×10^{17}	1×10^{18}	1×10^{18}	1×10^{18}	6.35×10^{17}	1×10^{18}	0	0	0	0	0
N_t (cm^{-3})	1×10^{14}	1×10^{14}	1×10^{15}	1×10^{15}	1×10^{15}	1×10^{15}	1×10^{15}	1×10^{14}	1×10^{15}	1×10^{15}	1×10^{15}
Ref.	15	26 and 27	26	28	29	30	27 and 31	15	32	33	34

shown in Fig. 2) of ETLs and HTLs with MPL. The CBO between MPL and ETLs, and VBO between MPL and HTLs indicate the condition of band alignment. For positive/negative values of VBO and CBO, a spike/cliff is established.[35] In the case of negative VBO, there is no hindrance of flowing holes to the back electrode. However, the increment of negative VBO gives rise to interfacial recombination. On the other hand, for negative CBO, the electron can simply drift to ETL.[36] However, for positive CBO (0–0.3 eV), low interfacial recombination and selective charge collection occurred.[14] The CBO and VBO calculated by using the following eqn (iv) and (v) are displayed in Table 4.

$$\text{CBO} = \chi_{\text{MPL}} - \chi_{\text{ETL}} \qquad (\text{iv})$$

$$\text{VBO} = (\chi_{\text{HTL}} + E_{\text{gHTL}}) - (\chi_{\text{MPL}} + E_{\text{gMPL}}) \qquad (\text{v})$$

where, $\chi_{\text{MPL}}/\chi_{\text{ETL}}/\chi_{\text{HTL}}$ is the electron affinity of MPL/ETL/HTL, respectively, and $E_{\text{gMPL}}/E_{\text{gHTL}}$ is band gap of MPL/HTL, respectively. Although CBO between MPL and WO$_3$ possesses the highest value than that for CBO between MPL and WS$_2$, better performance was exhibited by the structure with WS$_2$ as ETL. With the large band gap as well as the existence of valence band

maxima in relatively lower energy as compared to WS$_2$, it may create inhibition in hole transportation. As a result, it offers lower performance compared to the structure with WS$_2$.

From Tables 3 and TSI 01,† we have distinguished S4, S6, S16, S18, S22, S24, S28, S30, S34, S36, S40, and S42 as aspiring structures from 42 formulated structures according to their performance. S42 structure was the most satisfactory one among all the simulated devices, in which WS$_2$ and MoO$_3$ were utilized as ETL and HTL, respectively, and the obtained PPs were $V_{\text{OC}} = 1.09$ V, $J_{\text{SC}} = 20.71$ mA cm^{-2}, FF = 74.93%, and PCE = 23.10%. For further investigation of our research work, we extensively focused on optimizing the structure S42 by varying the different parameters of the layers.

3.1. Thickness optimization

The effect of changing MPL thickness was carried out from 300 nm to 700 nm while thicknesses of both ETL and HTL were sustained at 50 nm. The photovoltaic parameter J_{SC} was increased by 17.81% from the initial value. However, FF and V_{OC} were dropped 10.88% and 5.1%, respectively, from their original value owing to the change in MPL thickness. The decline

Table 3 Performance of various PSC structures

| Name of the structure	V_{oc} (V)	J_{sc} (mA cm^{-2})	FF (%)	η (%)
FTO/SnO$_2$/MPL/Spiro-OMeTAD/Au (S1)	0.96	20.09	53.84	14.12
FTO/SnO$_2$/MPL/Cu$_2$O/Au (S4)	1.09	20.42	64.60	19.64
FTO/SnO$_2$/MPL/MoO$_3$/Au (S6)	1.08	20.19	68.84	20.40
FTO/TiO$_2$/MPL/Cu$_2$O/Au (S16)	1.11	20.47	70.58	21.77
FTO/TiO$_2$/MPL/MoO$_3$/Au (S18)	1.09	20.22	75.13	22.58
FTO/ZnO/MPL/Cu$_2$O/Au (S22)	1.11	20.47	70.58	21.77
FTO/ZnO/MPL/MoO$_3$/Au (S24)	1.09	20.22	75.13	22.58
FTO/CdS MPL/Cu$_2$O/Au (S28)	1.11	20.51	70.31	21.70
FTO/CdS/MPL/MoO$_3$/Au (S30)	1.09	20.30	75.03	22.60
FTO/WO$_3$/MPL/Cu$_2$O/Au (S34)	1.11	20.48	70.59	21.79
FTO/WO$_3$/MPL/MoO$_3$/Au (S36)	1.09	20.25	75.12	22.61
FTO/WS$_2$/MPL/Cu$_2$O/Au (S40)	1.11	20.87	70.41	22.16
FTO/WS$_2$/MPL/MoO$_3$/Au (S42)	1.09	20.71	74.93	23.10
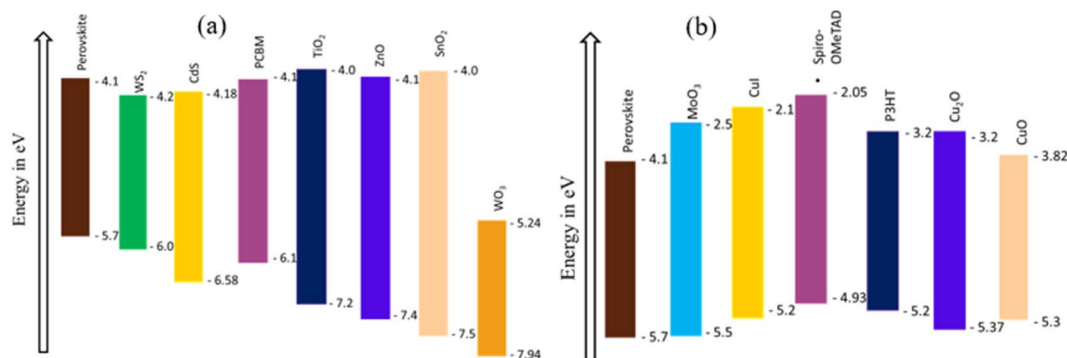
Fig. 2 Relative alignment of the energy band of $FA_{0.85}Cs_{0.15}Pb$ $(I_{0.85}Br_{0.15})_3$ (MPL) with (a) ETLs and (b) HTLs.[13–19]

Table 4 CBO and VBO of the MPL with ETLs and HTLs

ETL	PCBM	TiO$_2$	SnO$_2$	ZnO	CdS	WO$_3$	WS$_2$	HTL	Spiro-OMeTAD	P3HT	CuO	Cu$_2$O	CuI	MoO$_3$
CBO	−0.11	−0.01	0.09	−0.01	−0.09	0.29	0.14	VBO	−0.75	−0.48	−0.13	−0.31	−0.48	−0.18

meant that V_{OC} is happened due to the decrease in dark saturation current with the increase in thickness of the MPL.[37] In the case of FF, it showed declining behavior due to the increase in series resistance with the rise in the MPL thickness.[38] The positive gradient of current density at lower thickness is comparatively higher up to 450 nm after that the rate slowed down gradually. With increasing thickness, the absorption of a photon is more and consequently generates more electron–hole pairs. As a result, J_{SC} was eventually increased. After 450 nm thickness, rate of increasing J_{SC} becomes slow because of the dominating recombination rate.

Another important photovoltaic parameter, PCE increases with the increase in thickness of the MPL up to 450 nm at which maximum PCE was observed (23.45%) and then a slumping pattern was noticed till 700 nm. With the increasing thickness after 450 nm, PCE decreases due to the increase in series resistance and the recombination rate may also get higher owing to the lower diffusion length compared to the thickness.[39] The thickness of the MPL was optimized at 450 nm due to the aforementioned reason and the PPs were 1.08 V, 21.84 mA

cm^{-2}, 73.28%, and 23.45% for V_{OC}, J_{SC}, FF and PCE, respectively. Variations of PPs with respect to MPL thickness are displayed in Fig. 3.

The precise selection of parameters for ETL and HTL is crucial for fabricating highly efficient solar cells. The careful selection of ETL helps to minimize the recombination current and significantly enhances the transmittance, leading to improved overall performance.[40] To optimize the thickness of ETL, the thickness was changed from 10 nm to 100 nm and the thicknesses of the MPL and HTL were kept constant at 350 nm and 70 nm, respectively. The PCE of the device increased by 2.7% from the initial PCE of 22.66% and the change of other PPs was not a significant amount, which is displayed in Fig. FSI 1.† By considering the feasibility of the fabrication technique, we fixed the optimization value of ETL thickness at 50 nm. At 50 nm, the PPs for V_{OC}, J_{SC}, FF and PCE were 1.0924 V, 20.58317 mA cm^{-2}, 74.99%, and 22.97% respectively. Similarly, the thickness of the HTL was also varied from 10–100 nm by holding MPL thickness at 350 nm and ETL thickness at 50 nm. Owing to this, the change in PCE was noted slightly up to 50 nm,
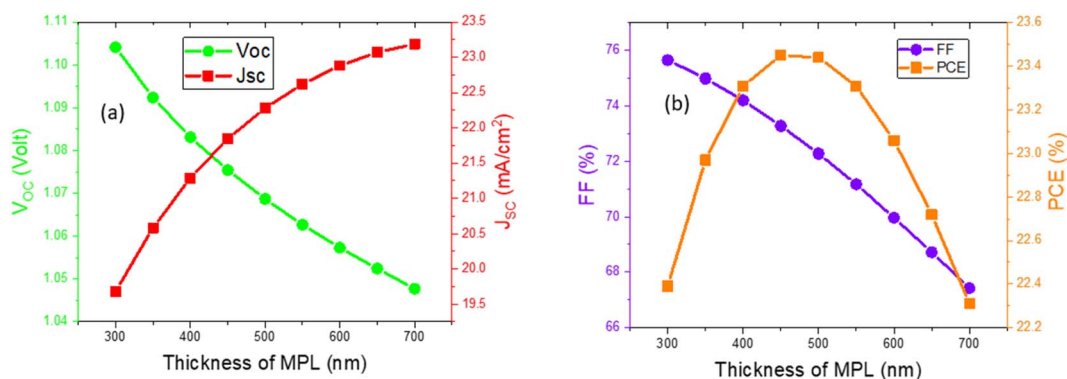

Fig. 3 Variation of the device characteristics, such as V_{OC}, J_{SC}, FF, and PCE with respect to the thickness of the MPL.

however, after 50 nm, the value was constant, which is displayed in Fig. FSI 2.† By analyzing the simulated data, the HTL thickness was optimized at 50 nm. From the clear inspection of our results, it is evident that the thickness of ETL and HTL imposes a very slight influence on the performance, which is also justified through previous works.[40,41]

3.2. Defects optimization

Defect density can be termed as a dominant parameter that deleteriously influences the performance of the device. The amount of charge carriers that can reach the respective electrode, which is initiated from the perovskite layer, greatly relies on this defect density. The recombination process is expedited with the increasing defect density at the perovskite layer. The relation between the recombination process to the defect density of the perovskite layer is illustrated by the Shockley–Read–Hall (SRH)[42] recombination model (vi) as follows;

$$R^{SRH} = \frac{v_{th}\sigma_n\sigma_p N_t(np - n_i^2)}{\sigma_n(n + n_1) + \sigma_p(p + p_1)} \qquad (vi)$$

where, v_{th} is the thermal velocity of charge carriers, σ_n/σ_p is the capture cross-section of electrons/holes, N_t is the number of defects per unit volume, n/p is the equilibrium electron/hole concentration, n_i is the intrinsic carrier concentration and n_1/p_1 is the concentration of electron/holes at trap states/valence band, respectively. The impact of the defect density on the lifetime of the carrier and diffusion length is explicated by the following eqn (vii) and (viii),[43]

$$\tau_{lifetime} = \frac{1}{\sigma\,N_t\,v_{th}} \qquad (vii)$$

$$L = \sqrt{\frac{\mu K_B T}{q}\tau_{lifetime}} \qquad (viii)$$

where, $\tau_{lifetime}$ is the lifetime of the charge carrier, L is the charge carrier diffusion length and μ is the mobility of the charge carrier.

To examine the impact of bulk defect density of MPL, the defect density was varied from 10^{10} cm^{-3} to 10^{15} cm^{-3}. All the PPs showed insignificant change with the bulk defect density and the PPs such as V_{OC}, J_{SC}, FF and PCE were changed by 1.6%, 0.17%, 1.32%, and 3.07%, respectively. The PPs were almost constant up to 10^{14} cm^{-3} bulk defect density. Hence 10^{14} cm^{-3} is termed as the tolerable bulk defect density of the structure. After that, the PPs decreased gradually with the increase in the defect density owing to the decrease in diffusion length, which results in increased bulk recombination as explained in the above equation. Variations of PPs owing to changing bulk defect density are shown in Fig. 4. Improving the crystalline quality and having a larger grain size have been proven to be advantageous to lessen the effect of the bulk defect. To perform this, photo-curing and thin-film post-processing can be employed.[44]

Interfacial trap density critically influences the PPs. In a perovskite material having a large absorption coefficient, photo-generated charge carrier numbers are high at the light illumination side compared to the backside. Interface recombination center has a greater impact on the probability of charge collection than severe recombination centers.

If light enters the perovskite structure through ETL, then the recombination rate at the ETL/perovskite layer interfaces is greater compared to the perovskite layer/HTL interfaces due to the generation of more electron–hole pairs. Poor interface quality severely influences the performance of the PSC. As a consequence of generating more electron–hole pairs in the ETL/perovskite layer interface because of light traveling from ETL to HTL *via* the absorbing layer, the rate of recombination was found higher in the ETL/perovskite layer interface than in the HTL/perovskite layer. For this reason, the ETL/perovskite interfacial layer is more sensitive. To analyze the effect of interfacial defects on the PPs, the interfacial trap density at WS$_2$/FA$_{0.85}$Cs$_{0.15}$Pb (I$_{0.85}$Br$_{0.15}$)$_3$ was varied from 10^{10} cm^{-3} to 10^{17} cm^{-3}. No appreciable change was noticed for the PPs up to 10^{15} cm^{-3}. After 10^{15} cm^{-3}, PCE starts to decrease gradually. Changes in PPs concerning the interfacial traps of WS$_2$/MPL are depicted in Fig. 5.

The interfacial trap density at FA$_{0.85}$Cs$_{0.15}$Pb (I$_{0.85}$Br$_{0.15}$)$_3$/MoO$_3$ was altered as well from 10^{10} cm^{-3} to 10^{15} cm^{-3} to visualize the impact on PPs. Variations of PPs for interfacial defects of MPL/MoO$_3$ are depicted in Fig. 6. The PPs remain unchanged up to 10^{13} cm^{-3} and after that, the PPs show a slight reduction. Because of the variation of interfacial defect density at ETL/MPL as well as MPL/HTL, reductions by 3.5% and 1.5% in PCE were
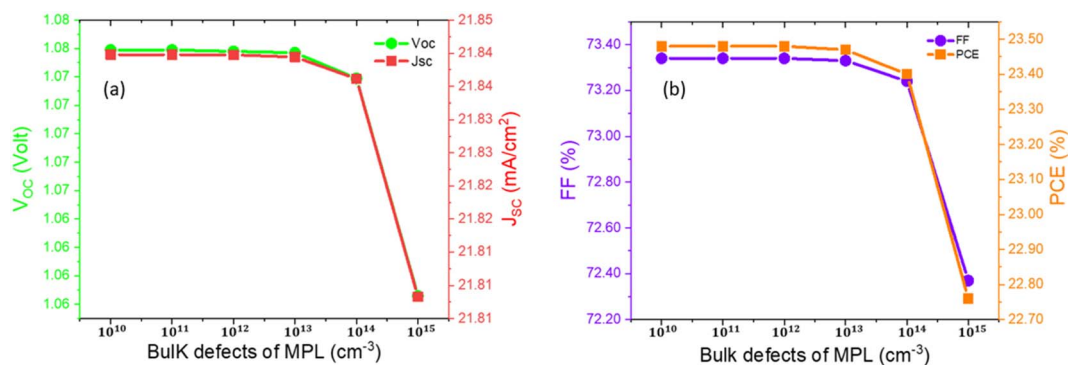

Fig. 4 Variation of the device characteristics, such as V_{OC}, J_{SC}, FF, and PCE with respect to bulk defects of the MPL.
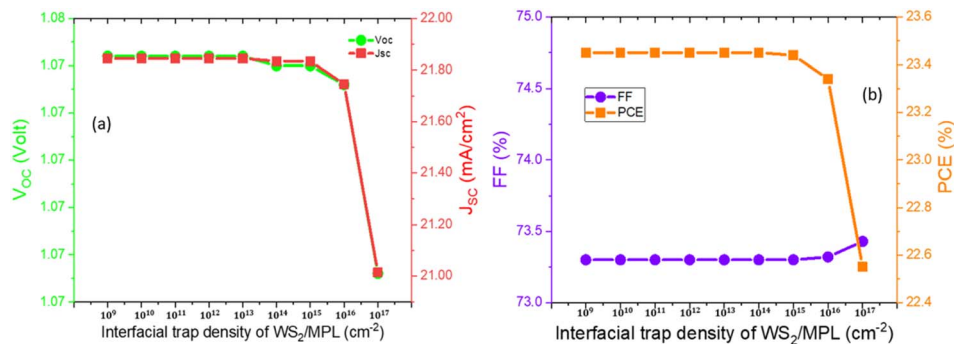
Fig. 5 Variation of the device characteristics, such as V_{OC}, J_{SC}, FF, and PCE with respect to the interfacial trap density of WS_2/MPL.
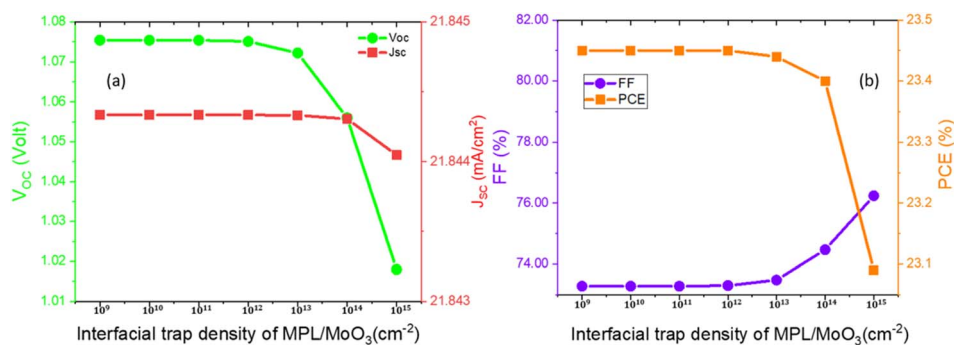

Fig. 6 Variation of the device characteristics, such as V_{OC}, J_{SC}, FF, and PCE with respect to the interfacial trap density of MPL/MoO_3.

detected, respectively. A greater recombination rate is the sole reason for the reduction in PPs with the increase in interfacial defect density. By weighing the above facts, 10^{15} cm^{-3}, and 10^{13} cm^{-3} were reckoned as the optimized interfacial trap density at ETL/MPL and MPL/HTL layers, respectively. To improve the band alignment between ETL/MPL and MPL/HTL layers, as well as to eradicate the defects and trap states in the interfacial layer, a buffer layer or additives with ETL or HTL can be a beneficial solution.[45,46] However, in both cases, the FF is slightly increased at the higher trap densities. To know the essence of this behavior of the FF parameter, further investigation is required.

3.3. Impact of defect density and thickness on quantum efficiency

The efficiency of the photovoltaic device can be calculated from IQE and EQE, where IQE refers to the total photocurrent generated under light illumination and EQE implies the optical performance of the PSC.[47–49] To realize the consequences of differing thickness on quantum efficiency, the MPL thickness was changed and the results are illustrated in Fig. 7a. For a thickness of 300 nm, the maximum quantum efficiency was 97.54% at a wavelength of 360 nm. Thickness range from 400 nm to 600 nm, the maximum quantum efficiency of about 99% was detected at 360 nm. An unnoticeable change of absorption has been observed after the 780 nm wavelength of light. All of our modeled structures showcased a noteworthy amount of QE, for the range of visible light. Our

proposed structure having a thickness of 450 nm, 98.8%, and 77.9% QE was assessed at wavelengths of 400 nm and 700 nm, respectively. Greater QE implied a larger collection of charge carriers, which signifies that our simulated structure demonstrated the best performance under visible light. The inspection was executed carefully to realize the outcome of altering the bulk density of MPL on QE by varying the bulk density from 10^{12} cm^{-3} to 10^{18} cm^{-3} and the obtained results are depicted in Fig. 7b. Approximately, 98.5% QE was encountered for defect density of up to 10^{16} cm^{-3} at a wavelength of 360 nm of light. However, the severe slump in QE was found after 10^{16} cm^{-3} and detection of 40% QE at 10^{18} cm^{-3} defect density in which the light wavelength was 690 nm. Unnoticeable absorption was observed after the 780 nm wavelength of light for all defect densities. In our proposed structure, having defect density of 10^{14} cm^{-3}, QE values were 99% to 78% at around 400 nm and 700 nm wavelength, respectively. Thus, this structure exhibits the best spectral response under visible light.

3.4. Capacitance–voltage characteristics of the PSC

The capacitance–voltage (C–V) technique can also be regarded as another salient technique for characterizing a solar cell by employing SCAPS-1D. Our present study emphasized exploring the outcome of ETL's N_D on C–V as well as the Mott–Schottky plot (M–S). Built-in potential, a foremost parameter, which is necessary for accumulating photo-generated holes and
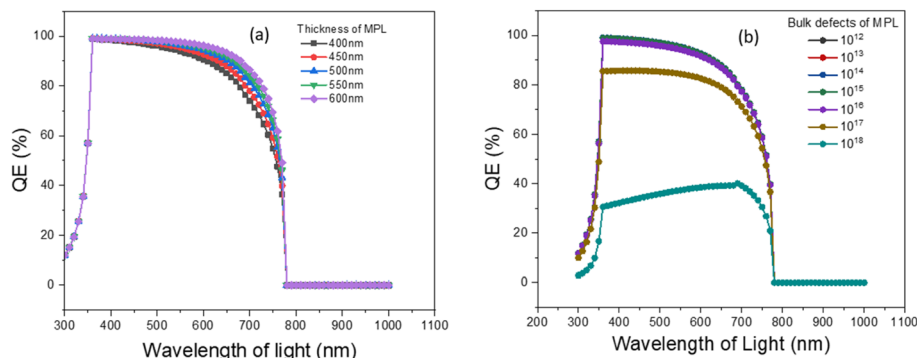

Fig. 7 Variation of QE owing to (a) thickness and (b) bulk defects of MPL.

electrons in opposite directions from each other, can be acquired from the M–S plot. The capacitance of a PSC can be correlated with the built-in potential by the following formula (ix),[50]

$$\frac{1}{C^2} = \frac{2}{A^2 \cdot \varepsilon \cdot q} \cdot \frac{1}{N_A} \cdot (V_{bi} - V) \quad (ix)$$

where V = applied voltage, V_{bi} = built-in potential, A = area, C = Capacitance, N_A = dopant density, and ε = permittivity of the vacuum medium.

Because of the influence of space charge, a larger capacitance value can be attained, which ultimately lowers the value of built-in potential. The recombination rate in a solar cell is notably lowered with the larger built-in potential, therefore, the attainment of greater PCE may be possible. After a definite range of voltage, the slope of capacitance can be negative. This negative capacitance may also be created from recombination or self-heating.

To probe the consequences of ETL's N_D on the $C–V$ and Mott–Schottky plots, this density was changed from 10^{17} cm^{-3} to 10^{20} cm^{-3} and the obtained results are mapped in Fig. 8. An identical graphical pattern for capacitance against voltage was found for all the varied donor densities, where, capacitance revealed exponentially increasing behavior with voltage until the approximate value of the voltage 0.78 V. This phenomenon

can be narrated as a large number of electrons being confined in the space charge region (SCR). In other words, a trivial amount of recombination of electron–hole pairs has happened in that region. After this certain value (0.78 V), capacitance manifested a sudden drop, offering a negative slope. The reason behind this can be ascribed in terms of the transformation of electron traps into hole traps in the SCR. According to the inspection of Burgelman et al.[51] on defect density, the lowering rate of electron density traps is equivalent to the growth rate of hole density traps in the SCR, which implies the alteration of electron traps into hole traps. The maximum capacitances were assessed as 13.23 nF cm^{-2}, 13.22 nF cm^{-2}, 13.20 nF cm^{-2}, and 13.09 nF cm^{-2} for uniform shallow donor densities of 10^{20} cm^{-3}, 10^{19} cm^{-3}, 10^{18} cm^{-3}, and 10^{17} cm^{-3}, respectively. From the scrutiny of the Mott–Schottky plot, the built-in potential was attained as 1.0 V to 0.85 V from the approximate intersection point at the horizontal axis for every graph with the N_D of 10^{17} cm^{-3} to 10^{20} cm^{-3}. Photo-generated holes and electrons can efficaciously proceed towards the respective electrode under the dominance of a larger built-in potential that finally provides us with higher conversion efficiency. In accordance with our inspection, the rising of donor density lowers the value of built-in potential owing to the elevation of the trapped electron in SCR that ultimately gives an increment in capacitance.
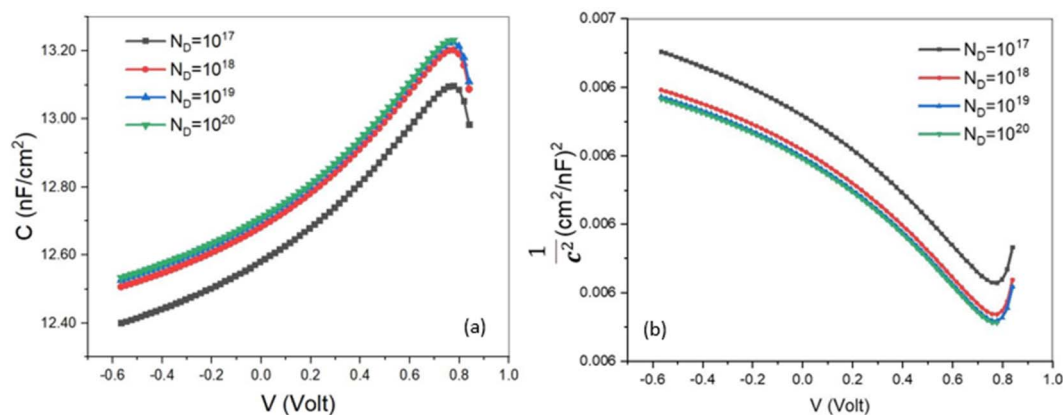

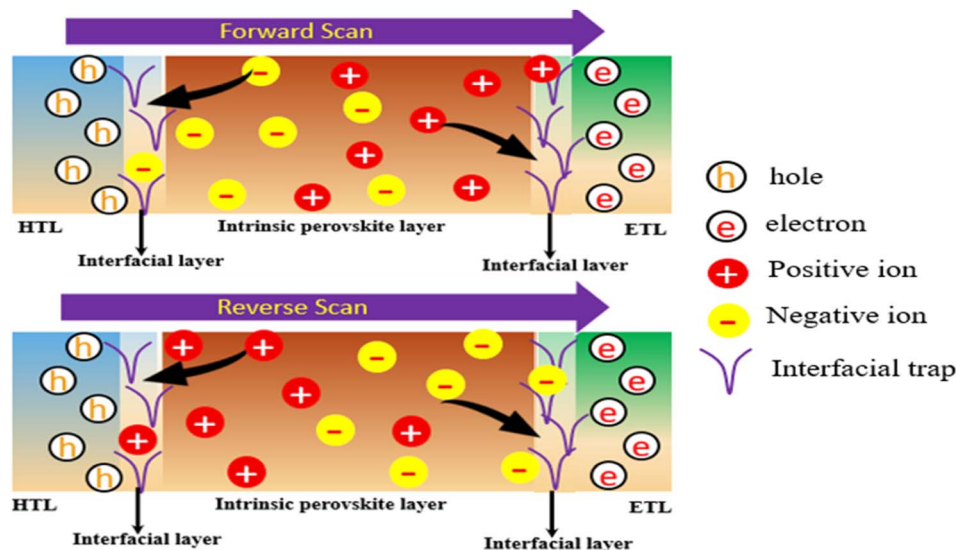Fig. 8 (a) $C–V$ characteristics and (b) MS plot as a function of ETL's N_D.

Fig. 9 A schematic of the charge migration and re-orientation in the perovskite layer under the influence of forward and reverse scans.
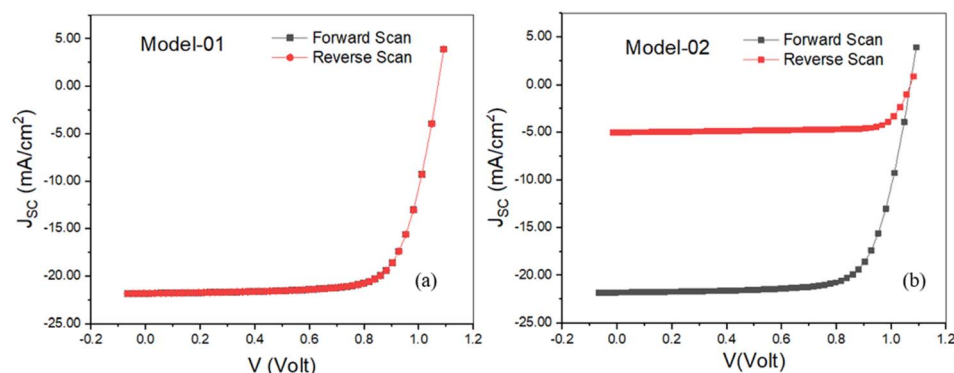

Fig. 10 Hysteresis effect on the J–V characteristics.

3.5. Hysteresis effect on the performance of the PSC

Ion migration and ion accumulation at the interfaces (portrayed in Fig. 9) under biasing voltage are one of the aspects involved in creating hysteresis in the J–V characteristics of a PSC.[52] Two types of models entitled Model-01 where ETL and HTL defects were termed as donor type and acceptor type defects, respectively, keeping the other defects as neutral type. In Model-02, defects of HTL/MPL, as well as MPL/ETL, were considered acceptor-type defects and donor-type defects, respectively, whereas MPL and FTO defects were considered neutral-type defects. In both cases, forward and reverse scans were examined by switching the defect type to investigate hysteresis behavior in the J–V curve. No hysteresis has been noticed in model-1, as shown in Fig. 10a. However, in model-2, the severe impact of hysteresis on the J–V curve was noted, as shown in Fig. 10b. Because of the influence of hysteresis, the amount of J_{SC} and PCE dropped to 76.94% and 75.40%, respectively, whereas V_{OC} showed a steady value in both cases and a slight increment in FF (6.7%) was pointed out as well.
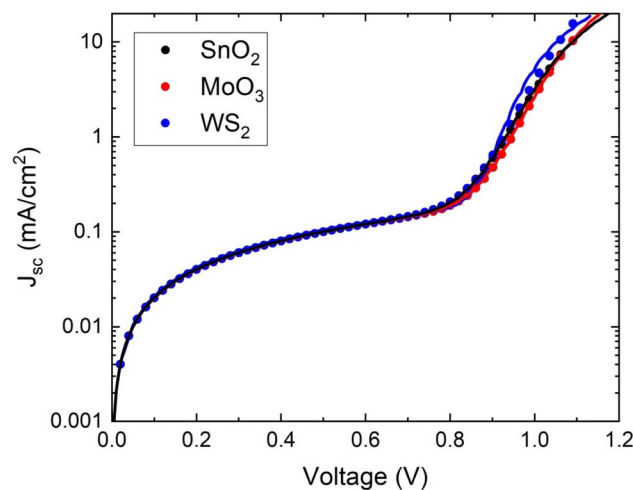

Fig. 11 Dark J–V characteristics of the perovskite solar cells used in model 1.

Table 5 Diode characteristics of three different ETL with perovskite structure FTO/ETL/FA$_{0.85}$Cs$_{0.15}$Pb(I$_{0.85}$Br$_{0.15}$)$_3$/MoO$_3$/Au

ETL	Saturation current density, I_0 (mA cm^{-2})	Ideality factor, n	Shunt resistance, R_{sh} (Ω cm^2)	Series resistance, R_s (Ω cm^2)
SnO$_2$	4.08×10^{-13}	1.38	4.96	0.00861
MoO$_3$	7.31×10^{-13}	1.36	4.99	0.00881
WS$_2$	1.09×10^{-14}	1.10	4.78	0.00797

As the interfacial layer is adjacent to the perovskite layer, ion accumulation and/or migration certainly have a significant influence on carrier transportation from perovskite to ETL and HTL. This could be the reason for generating the hysteresis effect in model 2. It has been reported that the J–V hysteresis in PSCs is caused by the localization of positively charged ions at the interface between the ETL and the perovskite layer.[53] Furthermore, the localized ions may accelerate non-radiative recombination, resulting in the rapid deterioration of PSCs.[53–55] Thus, to assure a reliable structure with the best performance, the proposed model-1 could be the best option.

3.6. Dark current analysis

The analysis of dark J–V for a photovoltaic device is an indispensable tool to realize the electrical characteristics in favor of the photovoltaic application. In the p–n junction, as a foundational cause of electronic noise, the dark current has been weighed.[56] As a consequence, the performance of the device was interjected. In the p–n junction, the dark current is indicated as the sum of the components of bulk and surface current.[57] The tunneling current, diffusion current, and generation–recombination current are part of the bulk component. The leakage shunt current and generation–recombination current are the components of the surface current, which in general appear at the interface of the semiconductor and dielectric devices.[57] The essence of the electrical properties of the PSC device can be deciphered by fitting dark J–V characteristics into a single p–n junction model. Fig. 11 shows the dark J–V curves of the optimized perovskite solar cell. The saturated current (I_0), series resistance (R_s), shunt resistance (R_{sh}) and ideality factor (n) are approximated by fitting the following equation onto the J–V characteristics of the proposed device.

$$I = I_0 \left[\exp\left(\frac{q(V - JR_s)}{nkT} \right) - 1 \right] + \frac{V - JR_s}{R_{sh}}$$

where k, q, and T are Boltzmann's constant, electronic charge, and temperature, respectively. The dark J–V curve has been plotted by utilizing the simulated data in which the data of current density are applied in logarithmic form (as shown in Figure). The diode characteristics, such as I_0, R_s, R_{sh}, and n of the three different solar cells were extrapolated, as shown in Table 5 by curve fitting using Origin 2018. It can be seen that the lowest saturated current density (I_0) of 1.09×10^{-14} mA cm^{-2} was found for the WS2; this lower value signifies that recombination (defect density) in the depletion region is quite insignificant[58] in this structure.

Moreover, the lowest series resistance 0.00797 Ω cm^2 for WS$_2$ is attributed to the superior charge transfer capability among the other ETL materials.[59] The ideality factor (n) of the device is a degree of assessment of how much a device is devoid of the ideal diode equation. The assessed ideality factors 1.38, 1.36 and 1.10 have been found for the SnO$_2$, MoO$_3$, and WS$_2$, which is the implication for the finer PCE and FF of the proposed solar cell. Finally, from the analysis of the dark J–V curve, the reasons behind the excellent photovoltaic parameters of our proposed structure are unraveled.

4. Conclusions

In our current study, compatible ETL and HTL for the MPL titled as FA$_{0.85}$Cs$_{0.15}$Pb (I$_{0.85}$Br$_{0.15}$)$_3$ were explored by utilizing multiple ETLs such as SnO$_2$, PCBM, TiO$_2$, ZnO, CdS, WO$_3$, and WS$_2$, and HTLs such as Spiro-OMeTAD, P3HT, CuO, Cu$_2$O, CuI, and MoO$_3$. Firstly, SnO$_2$ as ETL and Spiro-OMeTAD as HTL with the MPL were employed. Utilization of FTO as TCO and Au as a back metal electrode was performed to accomplish the structure as well. By keeping in mind the pragmatic factors, amphoteric defects (2×10^{15} cm^{-3}), interfacial defects (2×10^{10} cm^{-2} and 2×10^{11} cm^{-2} at HTL/MPL and MPL/ETL, respectively) and resistance ($R_s = 3 \Omega$ cm^2 and $R_{sh} = 5000 \Omega$ cm^2) were additionally placed in the structure along with IIPPs, which were theoretically and experimentally proven. The simulated results were $V_{OC} = 0.96$ V, $J_{SC} = 20.03$ mA cm^{-2}, FF = 53.84%, and PCE = 14.12%, which was harmonious with the experimentally substantiated data that also validate our simulation process. While the rest of the parameters and layers were kept invariable, with the variation of ETL and HTL, 42 structures were configured. S4, S6, S16, S18, S22, S24, S28, S30, S34, S36, S40, and S42 were picked out as propitious structures based on performance where S42 was the finest ones among all in which WS$_2$ and MoO$_3$ were applied as ETL and HTL, respectively. The obtained PPs for the structure S42 were $V_{OC} = 1.09$ V, $J_{SC} = 20.71$ mA cm^{-2}, FF = 74.93% and PCE = 23.10%. With the variation of the thickness of MPL, ETL, and HTL, bulk defects of MPL, and interfacial trap density, this structure was optimized. The optimized thicknesses of ETL, HTL, and MPL were 50 nm, 50 nm, and 450 nm, respectively. In addition, the tolerable bulk defects of MPL, interfacial defects of HTL/MPL, and MPL/ETL were assessed at 1×10^{14} cm^{-3}, 1×10^{13} cm^{-2} and 1×10^{15} cm^{-2}, respectively. The optimized PPs were $V_{OC} = 1.07$ V, $J_{SC} = 21.83$ mA cm^{-2}, FF = 73.41 and PCE = 23.39%. We performed the dark J–V analysis to unravel the reasons for the excellent photovoltaic parameters for the optimized structure of PSCs. From the dark J–V analysis, lower current density and series

resistance were observed, which is expectable for good solar cells. The ideality factor was assessed at 1.1, which attests to the better PCE and FF of the PSC. Monitoring of the QE of the structure was carried out by modifying the thickness and bulk defects of the MPL, and on average 88.5% QE was detected under visible light. The scanning of the C–V and Mott–Schottky plot was fulfilled by the modification of N_D. A declining nature of built-in potential and an increasing behavior in capacitance with the growth of N_D were observed. In the end, the assessment of the effect of hysteresis on the performance of the PSC was executed. Furthermore, the negative impact of hysteresis was investigated on the performance for model-2, and the decline of J_{SC} (76.94%) and PSC (75.4%) was noted, however, no hysteresis effect was noticed for model-1. For annulling this effect, the defect type should be neutral in the MoO_3/MPL and MPL/WS_2 interfaces as well as in MPL. With the command over the aforementioned parameters, remarkably efficient, as well as naturalistic PSC FTO/WS_2/$FA_{0.85}Cs_{0.15}Pb(I_{0.85}Br_{0.15})_3$/$MoO_3$/Au can be fabricated.

Data availability

Data will be available from the corresponding author upon request.

Author contributions

The conceptualization and simulation were carried out by M H Miah and M B Rahman. M H Miah, M B Rahman, and Noor-E-Ashrafi led the manuscript writing effort, with support from M A Islam and M U Khandaker. Review and editing supported by M A Islam. M A Islam supervised the research. The findings were discussed by all contributors, and they all contributed to the final manuscript.

Conflicts of interest

There are no conflicts of interest.

Acknowledgements

References

1 F. Behrouznejad, S. Shahbazi, N. Taghavinia, H.-P. Wu and E. Wei-Guang Diau, A study on utilizing different metals as the back contact of CH3NH3PbI3 perovskite solar cells, *J. Mater. Chem. A*, 2016, **4**, 13488–13498.

2 I. Alam, R. Mollick and M. A. Ashraf, Numerical simulation of Cs2AgBiBr6-based perovskite solar cell with ZnO nanorod and P3HT as the charge transport layers, *Phys. B*, 2021, **618**, 413187.

3 A. Kojima, K. Teshima, Y. Shirai and T. Miyasaka, Organometal Halide Perovskites as Visible-Light Sensitizers for Photovoltaic Cells, *J. Am. Chem. Soc.*, 2009, **131**, 6050–6051.

4 H. Min, D. Y. Lee, J. Kim, G. Kim, K. S. Lee, J. Kim, *et al.*, Perovskite solar cells with atomically coherent interlayers on SnO2 electrodes, *Nature*, 2021, **598**, 444–450.

5 M. Green, E. Dunlop, J. Hohl-Ebinger, M. Yoshita, N. Kopidakis and X. Hao, Solar cell efficiency tables (version 57), *Prog. Photovolt.: Res. Appl.*, 2021, **29**, 3–15.

6 M. H. Miah, M. B. Rahman, M. Nur-E-Alam, N. Das, N. B. Soin, S. F. W. M. Hatta, *et al.*, Understanding the Degradation Factors, Mechanism and Initiatives for Highly Efficient Perovskite Solar Cells, *ChemNanoMat*, 2023, **9**, e202200471.

7 C. Liu, Y. Yang, X. Xia, Y. Ding, Z. Arain, S. An, *et al.*, Soft Template-Controlled Growth of High-Quality CsPbI3 Films for Efficient and Stable Solar Cells, *Adv. Energy Mater.*, 2020, **10**, 1903751.

8 M. Saliba, T. Matsui, J.-Y. Seo, K. Domanski, J.-P. Correa-Baena, M. K. Nazeeruddin, *et al.*, Cesium-containing triple cation perovskite solar cells: improved stability, reproducibility and high efficiency, *Energy Environ. Sci.*, 2016, **9**, 1989–1997.

9 C. Liu, J. Sun, W. L. Tan, J. Lu, T. R. Gengenbach, C. R. McNeill, *et al.*, Alkali Cation Doping for Improving the Structural Stability of 2D Perovskite in 3D/2D PSCs, *Nano Lett.*, 2020, **20**, 1240–1251.

10 M. K. Hossain, M. H. K. Rubel, G. I. Toki, I. Alam, M. F. Rahman and H. Bencherif, Effect of various electron and hole transport layers on the performance of CsPbI3-based perovskite solar cells: A numerical investigation in DFT, SCAPS-1D, and wxAMPS frameworks, *ACS Omega*, 2022, **7**, 43210–43230.

11 S. K. Pathak, A. Abate, P. Ruckdeschel, B. Roose, K. C. Gödel, Y. Vaynzof, *et al.*, Performance and Stability Enhancement of Dye-Sensitized and Perovskite Solar Cells by Al Doping of TiO2, *Adv. Funct. Mater.*, 2014, **24**, 6046–6055.

12 J. Song, E. Zheng, J. Bian, X.-F. Wang, W. Tian, Y. Sanehira, *et al.*, Low-temperature SnO 2-based electron selective contact for efficient and stable perovskite solar cells, *J. Mater. Chem. A*, 2015, **3**, 10837–10844.

13 S. Karthick, S. Velumani and J. Bouclé, Experimental and SCAPS simulated formamidinium perovskite solar cells: A comparison of device performance, *Sol. Energy*, 2020, **205**, 349–357.

14 S. Ahmed, F. Jannat, M. A. K. Khan and M. A. Alim, Numerical development of eco-friendly Cs2TiBr6 based perovskite solar cell with all-inorganic charge transport materials *via* SCAPS-1D, *Optik*, 2021, **225**, 165765.

15 M. Mottakin, K. Sobayel, D. Sarkar, H. Alkhammash, S. Alharthi, K. Techato, *et al.*, Design and Modelling of Eco-Friendly CH3NH3SnI3-Based Perovskite Solar Cells with Suitable Transport Layers, *Energies*, 2021, **14**, 7200.

16 Y. Gan, X. Bi, Y. Liu, B. Qin, Q. Li, Q. Jiang, et al., Numerical investigation energy conversion performance of tin-based perovskite solar cells using cell capacitance simulator, Energies, 2020, 13, 5907.

17 A. Singh, P.-T. Lai, A. Mohapatra, C.-Y. Chen, H.-W. Lin, Y.-J. Lu, et al., Panchromatic heterojunction solar cells for Pb-free all-inorganic antimony based perovskite, Chem. Eng. J., 2021, 419, 129424.

18 K. Sobayel, M. Akhtaruzzaman, K. S. Rahman, M. T. Ferdaous, Z. A. Al-Mutairi, H. F. Alharbi, et al., A comprehensive defect study of tungsten disulfide (WS2) as electron transport layer in perovskite solar cells by numerical simulation, Results Phys., 2019, 12, 1097–1103.

19 A. Raj, M. Kumar, H. Bherwani, A. Gupta and A. Anshul, Evidence of improved power conversion efficiency in lead-free CsGeI3 based perovskite solar cell heterostructure via scaps simulation, J. Vac. Sci. Technol., B: Nanotechnol. Microelectron.: Mater., Process., Meas., Phenom., 2021, 39, 012401.

20 H.-S. Kim, C.-R. Lee, J.-H. Im, K.-B. Lee, T. Moehl, A. Marchioro, et al., Lead Iodide Perovskite Sensitized All-Solid-State Submicron Thin Film Mesoscopic Solar Cell with Efficiency Exceeding 9%, Sci. Rep., 2012, 2, 591.

21 Z.-L. Tseng, L.-C. Chen, C.-H. Chiang, S.-H. Chang, C.-C. Chen and C.-G. Wu, Efficient inverted-type perovskite solar cells using UV-ozone treated MoOx and WOx as hole transporting layers, Sol. Energy, 2016, 139, 484–488.

22 Y. Gong, Y. Dong, B. Zhao, R. Yu, S. Hu and Z. a. Tan, Diverse applications of MoO3 for high performance organic photovoltaics: fundamentals, processes and optimization strategies, J. Mater. Chem. A, 2020, 8, 978–1009.

23 M. Burgelman, K. Decock, A. Niemegeers, J. Verschraegen, and S. Degrave, SCAPS Manual, February, 2016.

24 F. Liu, J. Zhu, J. Wei, Y. Li, M. Lv, S. Yang, et al., Numerical simulation: Toward the design of high-efficiency planar perovskite solar cells, Appl. Phys. Lett., 2014, 104, 253508.

25 S. Zandi, P. Saxena, M. Razaghi and N. E. Gorji, Simulation of CZTSSe Thin-Film Solar Cells in COMSOL: Three-Dimensional Optical, Electrical, and Thermal Models, IEEE J. Photovolt., 2020, 10, 1503–1507.

26 N. Lakhdar and A. Hima, Electron transport material effect on performance of perovskite solar cells based on CH3NH3GeI3, Opt. Mater., 2020, 99, 109517.

27 M. Chen, M.-G. Ju, A. D. Carl, Y. Zong, R. L. Grimm, J. Gu, et al., Cesium titanium (IV) bromide thin films based stable lead-free perovskite solar cells, Joule, 2018, 2, 558–570.

28 M. M. Salah, K. M. Hassan, M. Abouelatta and A. Shaker, A comparative study of different ETMs in perovskite solar cell with inorganic copper iodide as HTM, Optik, 2019, 178, 958–963.

29 Y. Zhang and P. W. M. Blom, Electron and hole transport in poly(fluorene-benzothiadiazole), Appl. Phys. Lett., 2011, 98, 143504.

30 N. Rai, S. Rai, P. K. Singh, P. Lohia and D. Dwivedi, Analysis of various ETL materials for an efficient perovskite solar cell by numerical simulation, J. Mater. Sci.: Mater. Electron., 2020, 31, 16269–16280.

31 E. Karimi and S. Ghorashi, Investigation of the influence of different hole-transporting materials on the performance of perovskite solar cells, Optik, 2017, 130, 650–658.

32 S. Rai, B. K. Pandey, A. Garg and D. K. Dwivedi, Hole transporting layer optimization for an efficient lead-free double perovskite solar cell by numerical simulation, Opt. Mater., 2021, 121, 111645.

33 S. Pitchaiya, M. Natarajan, A. Santhanam, V. Asokan, A. Yuvapragasam, V. M. Ramakrishnan, et al., A review on the classification of organic/inorganic/carbonaceous hole transporting materials for perovskite solar cell application, Arabian J. Chem., 2020, 13, 2526–2557.

34 W. Li, W. Li, Y. Feng and C. Yang, Numerical analysis of the back interface for high efficiency wide band gap chalcopyrite solar cells, Sol. Energy, 2019, 180, 207–215.

35 A. Mohandes, M. Moradi and H. Nadgaran, Numerical simulation of inorganic Cs2AgBiBr6 as a lead-free perovskite using device simulation SCAPS-1D, Opt. Quantum Electron., 2021, 53, 319.

36 T. Minemoto and M. Murata, Theoretical analysis on effect of band offsets in perovskite solar cells, Sol. Energy Mater. Sol. Cells, 2015, 133, 8–14.

37 A. Zekry, A. Shaker and M. Salem, Solar cells and arrays: principles, analysis, and design, in Advances in renewable energies and power technologies, Elsevier, 2018, pp. 3–56.

38 W. Abdelaziz, A. Shaker, M. Abouelatta and A. Zekry, Possible efficiency boosting of non-fullerene acceptor solar cell using device simulation, Opt. Mater., 2019, 91, 239–245.

39 F. Jannat, S. Ahmed and M. A. Alim, Performance analysis of cesium formamidinium lead mixed halide based perovskite solar cell with MoOx as hole transport material via SCAPS-1D, Optik, 2021, 228, 166202.

40 K. Shivesh, I. Alam, A. K. Kushwaha, M. Kumar and S. V. Singh, Investigating the theoretical performance of Cs2TiBr6-based perovskite solar cell with La-doped BaSnO3 and CuSbS2 as the charge transport layers, Int. J. Energy Res., 2022, 46, 6045–6064.

41 M. K. Hossain, G. I. Toki, I. Alam, R. Pandey, D. Samajdar, M. F. Rahman, et al., Numerical simulation and optimization of a CsPbI 3-based perovskite solar cell to enhance the power conversion efficiency, New J. Chem., 2023, 47, 4801–4817.

42 B. MaríSoucase, I. G. Pradas, and K. R. Adhikari, Numerical simulations on perovskite photovoltaic devices, Perovskite materials: synthesis, characterisation, properties, and applications, 2016, vol. 445.

43 M. A. Green, Solar cells: operating principles, technology, and system applications, Englewood Cliffs, 1982.

44 F. Wang, S. Bai, W. Tress, A. Hagfeldt and F. Gao, Defects engineering for high-performance perovskite solar cells, npj Flexible Electron., 2018, 2, 22.

45 J. Du, L. Feng, X. Guo, X. Huang, Z. Lin, J. Su, et al., Enhanced efficiency and stability of planar perovskite solar cells by introducing amino acid to SnO2/perovskite interface, J. Power Sources, 2020, 455, 227974.

46 S. Guarnera, A. Abate, W. Zhang, J. M. Foster, G. Richardson, A. Petrozza, et al., Improving the Long-Term Stability of

Perovskite Solar Cells with a Porous Al2O3 Buffer Layer, *J. Phys. Chem. Lett.*, 2015, **6**, 432–437.

47 K. Chakraborty, M. G. Choudhury and S. Paul, Numerical study of Cs2TiX6 (X= Br⁻, I⁻, F⁻ and Cl⁻) based perovskite solar cell using SCAPS-1D device simulation, *Sol. Energy*, 2019, **194**, 886–892.

48 X. Wang, T. Zhang, Y. Lou and Y. Zhao, All-inorganic lead-free perovskites for optoelectronic applications, *Mater. Chem. Front.*, 2019, **3**, 365–375.

49 M. Helal Miah, M. Bulu Rahman, F. Khatun, M. U. Khandaker, S. F. Wan Muhammad Hatta, N. B. Soin, *et al.*, Optimization and detail analysis of novel structure Pb- free CsGeI3-based all-inorganic perovskite solar cells by SCAPS-1D, *Optik*, 2023, 170819.

50 T. Kirchartz, W. Gong, S. A. Hawks, T. Agostinelli, R. C. I. MacKenzie, Y. Yang, *et al.*, Sensitivity of the Mott–Schottky Analysis in Organic Solar Cells, *J. Phys. Chem. C*, 2012, **116**, 7672–7680.

51 M. Burgelman, F. Engelhardt, J. Guillemoles, R. Herberholz, M. Igalson, R. Klenk, *et al.*, Defects in Cu (In, Ga) Se2 semiconductors and their role in the device performance of thin-film solar cells, *Prog. Photovolt.: Res. Appl.*, 1997, **5**, 121–130.

52 A. Kumar, Numerical modelling of ion-migration caused hysteresis in perovskite solar cells, *Opt. Quantum Electron.*, 2021, **53**, 166.

53 S. A. Weber, I. M. Hermes, S.-H. Turren-Cruz, C. Gort, V. W. Bergmann, L. Gilson, *et al.*, How the formation of interfacial charge causes hysteresis in perovskite solar cells, *Energy Environ. Sci.*, 2018, **11**, 2404–2413.

54 T. S. Sherkar, C. Momblona, L. Gil-Escrig, J. Avila, M. Sessolo, H. J. Bolink, *et al.*, Recombination in perovskite solar cells: significance of grain boundaries, interface traps, and defect ions, *ACS Energy Lett.*, 2017, **2**, 1214–1222.

55 K. Domanski, B. Roose, T. Matsui, M. Saliba, S.-H. Turren-Cruz, J.-P. Correa-Baena, *et al.*, Migration of cations induces reversible performance losses over day/night cycling in perovskite solar cells, *Energy Environ. Sci.*, 2017, **10**, 604–613.

56 Y. Jiao, G. Lu, Y. Feng, C. Zhang, W. Wang, S. Wu, *et al.*, Towards high sensitivity infrared detector using Cu2CdxZn1-xSnSe4 thin film by SCAPS simulation, *Sol. Energy*, 2021, **225**, 375–381.

57 K. R. Linga, G. H. Olsen, V. S. Ban, A. N. Joshi and W. F. Kosonocky, Dark current analysis and characterization of In/sub x/Ga/sub 1-x/As/InAs/sub y/P/sub 1-y/graded photodiodes with x>0.53 for response to longer wavelengths (>1.7 mu m), *J. Lightwave Technol.*, 1992, **10**, 1050–1055.

58 M. A. Islam, H. Mohafez, K. Sobayel, S. F. Wan Muhamad Hatta, A. K. M. Hasan, M. U. Khandaker, *et al.*, Degradation of Perovskite Thin Films and Solar Cells with Candle Soot C/Ag Electrode Exposed in a Control Ambient, *Nanomaterials*, 2021, **11**, 3463.

59 R. T. Ginting, M.-K. Jeon, K.-J. Lee, W.-Y. Jin, T.-W. Kim and J.-W. Kang, Degradation mechanism of planar-perovskite solar cells: correlating evolution of iodine distribution and photocurrent hysteresis, *J. Mater. Chem. A*, 2017, **5**, 4527–4534.